

Received June 8, 2018, accepted July 8, 2018, date of publication July 20, 2018, date of current version August 20, 2018.

Digital Object Identifier 10.1109/ACCESS.2018.2858199

Using High-Control-Bandwidth FPGA and SiC Inverters to Enhance High-Frequency Injection Sensorless Control in Interior Permanent Magnet Synchronous Machine

WEI QIAN^{1,2}, XI ZHANG¹, FANNING JIN², (Student Member, IEEE),
HUA BAI³, (Member, IEEE), DINGGUO LU⁴, (Member, IEEE),
AND BING CHENG⁴, (Member, IEEE)

¹School of Mechanical Engineering, Shanghai Jiaotong University, Shanghai 200240, China

²Department of Electrical and Computer Engineering, University of Michigan-Dearborn, Dearborn, MI 48128, USA

³Department of Electrical Engineering and Computer Science, University of Tennessee, Knoxville, TN 37996, USA

⁴Mercedes Benz North America, Redford Charter Twp, MI 48239, USA

Corresponding authors: Xi Zhang (braver1980@sjtu.edu.cn) and Hua Bai (hbai2@utk.edu)

This work was supported in part by the Mercedes-Benz North America, in part by the National Science Fund of China under Grant 51677118, in part by the National Key Research and Development Plan Key Special Project under Grant 2017YFE0102000, and in part by the Shanghai Municipal Inter-Governmental International Collaboration Project under Grant 16510711500.

ABSTRACT A high-frequency injection (HFI) sensorless control for interior permanent magnet synchronous motors with enhanced precision and widened speed range is proposed in this paper. The injection frequency reaches up to 2 kHz under a 50~100 kHz silicon carbide (SiC)-based three-phase inverter. In addition to the high switching frequency, the field-programmable gate array (FPGA) is utilized to achieve high control bandwidth (>200 kHz) when implementing the field-oriented control algorithm. The benefits of high switching frequency and high control bandwidth in senseless controls are explained theoretically, i.e., leaving enough room for the injection frequency by using SiC while tuning down the noise-to-signal ratio by using the FPGA. Experimental results verified that such manners improved the position estimation and lifted the injection frequency effectively, which further allows us to widen the motor speed range under the HFI sensorless control from 0 to 500 r/min with the conventional Si+DSP design to 0~1200 r/min with the proposed SiC+FPGA.

INDEX TERMS Field-oriented control, FPGA, interior PMSM, sensorless, SiC.

I. INTRODUCTION

Due to the prevalence of Electric Vehicles (EVs), the high-power level multiple pole-pair permanent magnet synchronous motor (PMSM) is receiving more attention than ever [1], where field-oriented control (FOC) is commonly used [2]. Traditional design flow uses microcontrollers such as Digital Signal Processor (DSP) and PowerPC. However, in some cases that require a lot of computation resources such as the sensorless motor control, one single microcontroller is not sufficient. With most of microcontrollers implementing control algorithms in serial sequence, the control bandwidth, i.e., the updating rate of the Pulse-Width Modulation (PWM) duty cycles, is highly limited. This explains why the PWM updating rate is usually lower than the switching frequency, especially when the switching frequency is high.

There are several candidate sensorless control methods for interior permanent magnet synchronous motors (IPMSMs), e.g., high-frequency signal injection, back EMF estimation, model-based adaptive method, Kalman observer and sliding mode observer. The back EMF method is not competent for the angle estimation at the low speed, where the back EMF is weak [3]–[8]. The model reference adaptive rule has high dependence on parameters of the motor. The Kalman filter observation is resource occupying and complex, and it also has high dependence on parameters of the motor [9], [10]. The sliding mode control is a non-continuous system because of its observer. “Chattering” of the system is hard to avoid, which seriously affects the accuracy and reliability of the system. It is rare to apply in EVs yet.

The high-frequency injection (HFI) method, at the present stage, is one of very few methods with angle estimations applicable to zero or low speed. For such method, the precision of the angle estimation and the effective range of the motor speed are always top concerns [11]–[16]. Reference [11], [12], and [13] described how a HFI technique is used on IPMSMs to extract the rotor position information from the inherent saliency of the machine. Reference [14] has proposed a scheme by using a saturated flux linkage model to distinguish the polarity of the rotor magnet at the standstill. However, most of works focused on the low injection frequency and low speed estimation.

Another high-frequency injection method is the square-wave signal injection [17]–[21], which has received attention in recent years. It is suitable for applications with the high dynamic response. In applications where low noise and low machine saturation effect are demanded, the sinusoidal injection is more suitable [21].

Some researchers proposed the hybrid sensorless position estimation [22]–[24] for a wider range of the motor speed. However the accuracy of the position estimation is limited by either the switching frequency or the microcontroller. Reference [25] presented a Sliding Mode Observer (SMO) to extend the range of speed, while the precision is still very low due to the low switching frequency (5 kHz). In [26], current control algorithm is carried out every 100 μs. The switching frequency of the inverter and control bandwidth of the algorithm are low. The error reached 0.4 rad. In [27], the inverter uses the switching frequency of 5 kHz, and the estimated algorithm is running at 450 rpm electrical angle. In [28], the controller of PMSM uses Field Programmable Gate Arrays (FPGAs), the switching frequency is 6 kHz, HF signal is 1.2 kHz, the test speed is 100rpm, and the error also reaches 0.4 rad.

Authors of this paper believe the switching frequency and control bandwidth are the two critical impact factors of the HFI control. To further enhance the HFI performance, a high control-bandwidth microcontroller such as FPGA, and a high-switching-frequency inverter such as with SiC devices are musts. Essentially various functional modules inside the FPGA can be implemented in parallel instead of in series, which results in the updating rate of the FOC loop up to hundreds of kHz, in contrast to 10 kHz of the conventional EV inverter. This potentially results in updating the duty cycle of each switch every switching period, yielding a faster control response and close to ideal sinusoidal motor current waveform [29]–[32]. When combined with high-switching-frequency SiC devices [33], [34], the motor drive inverter system in this study expects a superior-performing HFI sensorless control, i.e., 1) the ultra-high switching frequency resulted from SiC devices allows the increment of the injection frequency, distant the injected signal away from the fundamental signal thereby facilitating the signal extraction, which meanwhile reduces the audible noise, 2) by increasing the control bandwidth through the adoption of FPGAs, the switch duty cycle will be updated every switching

period, which reduces the distortion of fundamental and injection signals and further improves the position estimation, and 3) the increment of the injection frequency also allows the Low-Pass Filter (LPF) to design a cut-off frequency distant from the fundamental signal, which decouples the fundamental back EMF from the HFI signal thereby widening the motor speed range applying HFI sensorless control. All these assumptions need further verification in this paper.

The rest of this paper is organized as follows. Section II analyzed impact factors of the HFI sensorless estimation method, particularly the control bandwidth and switching frequency. Section III provided the system modeling based on Xilinx System Generator (XSG), a Fixed-Point Arithmetic toolbox to automatically generate the HDL code for Xilinx 7K325 FPGA chip embedded in dSPACE MicroAutobox, as the foundation to realize the sensorless control. Section IV presented hardware implementation and experimental results. Section V concluded the contribution and innovation of this paper.

II. HFI SENSORLESS CONTROL VS CONTROL BANDWIDTH AND SWITCHING FREQUENCY

Fig. 1 is a schematic diagram of a three-phase IPM drive, with its mathematical model in the d-q reference frame described by (1).

$$\begin{cases} V_{ds} = R_s i_{ds} + L_d \frac{di_{ds}}{dt} - \omega_r L_q i_{qs} \\ V_{qs} = R_s i_{qs} + L_q \frac{di_{qs}}{dt} + \omega_r L_d i_{ds} + \omega_r \psi_m \end{cases} \quad (1)$$

where V_{ds} , V_{qs} , i_{ds} , i_{qs} are the stator d-axis and q-axis voltage and current, respectively. R_s is the stator resistance, L_d , L_q are the d- and q- axis inductance, respectively, ω_r is the angular velocity, and Ψ_m is the magnet flux linkage.

The d-q currents are obtained using Park transformation.

$$\begin{bmatrix} i_q \\ i_d \\ i_0 \end{bmatrix} = \begin{bmatrix} \cos \theta_r & \cos(\theta_r - \frac{2\pi}{3}) & \cos(\theta_r + \frac{2\pi}{3}) \\ \sin \theta_r & \sin(\theta_r - \frac{2\pi}{3}) & \sin(\theta_r + \frac{2\pi}{3}) \\ \frac{1}{2} & \frac{1}{2} & \frac{1}{2} \end{bmatrix} \begin{bmatrix} i_a \\ i_b \\ i_c \end{bmatrix} \quad (2)$$

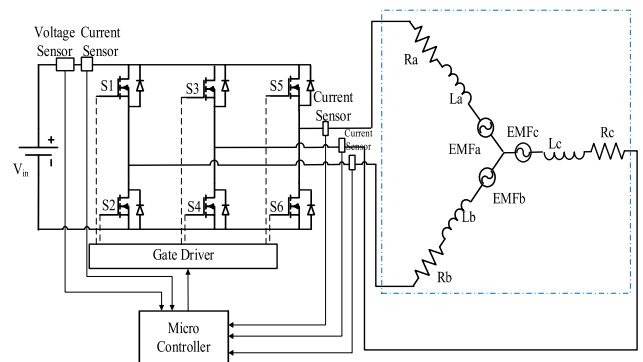


FIGURE 1. The equivalent circuit schematic of the PMSM drive system.

A. HFI MODEL

The frequency of the injected signal needs be higher than the fundamental frequency. The relationship between the injected voltage and current can be approximated as (3).

$$\begin{cases} V_{dc} = L_d \frac{di_{dc}}{dt} \\ V_{qc} = L_q \frac{di_{qc}}{dt} \end{cases} \quad (3)$$

The subscript *c* denotes injected variables. The IPMSM is well suited for the HFI technique to track a spatial saliency, because of the inductance difference between d and q axis in the rotor reference frame. The HFI method superimposes a d-axis sinusoidal carrier signal in the estimated rotor reference frame onto the fundamental component voltage. Specifically, the injected high frequency voltage complies with

$$\begin{cases} \hat{V}_{dc} = V_c \cos \omega_c t \\ \hat{V}_{qc} = 0 \end{cases} \quad (4)$$

The $\hat{\cdot}$ denotes the variable in the estimated d-q frame. Furthermore, the current in the estimated rotor reference frame can be expressed as follows.

$$\begin{cases} \hat{i}_{dc} = \frac{V_c}{2\omega_c} \left[\left(\frac{1}{L_d} + \frac{1}{L_q} \right) + \left(\frac{1}{L_d} - \frac{1}{L_q} \right) \cos 2(\theta_r - \hat{\theta}_r) \right] \sin \omega_c t \\ \quad + \frac{V_c^2}{2\omega_c^2} \frac{d^2 i_d}{d\psi_d^2} (\psi_d) \cos^3(\theta_r - \hat{\theta}_r) \sin^2 \omega_c t \\ \hat{i}_{qc} = \frac{V_c}{2\omega_c} \left(\frac{1}{L_d} - \frac{1}{L_q} \right) \sin 2(\theta_r - \hat{\theta}_r) \sin \omega_c t \\ \quad + \frac{V_c^2}{2\omega_c^2} \frac{d^2 i_d}{d\psi_d^2} (\psi_d) \cos^2(\theta_r - \hat{\theta}_r) \sin(\theta_r - \hat{\theta}_r) \sin^2 \omega_c t \end{cases} \quad (5)$$

where θ_r and $\hat{\theta}_r$ denote the actual and estimated rotor position, respectively. From (5), the first item of q-axis current is suitable for the position detection, and the second item of the d-axis current is suitable for the polarity identification. Fig. 2 shows the heterodyning process to extract the position and polarity information. (6) shows the position error term, which has an approximate linear relationship with the error between the actual and estimated angle. This error term will be used as the input of a PLL based tracking controller to drive the estimated angle to the true value. (7) shows the polarity signal term.

$$\begin{aligned} Err_{pos} &= LPF\{\hat{i}_{qsc} \sin \omega_c t\} \\ &= \frac{V_c}{4\omega_c} \left(\frac{L_q - L_d}{L_d L_q} \right) \sin 2(\theta_r - \hat{\theta}_r) \end{aligned} \quad (6)$$

$$\begin{aligned} Sign_{pol} &= LPF\{\hat{i}_{dsc} \cos 2\omega_c t\} \\ &= -\frac{V_c^2}{8\omega_c^2} \frac{d^2 i_d}{d\psi_d^2} (\psi_m) \cos^3(\theta_r - \hat{\theta}_r) \end{aligned} \quad (7)$$

The demodulated error signal is an input, which goes into a PI regulator and is ultimately fed back to form a closed loop. Fig. 3 shows the tracking loop used for the rotor position estimation, where ω_{HF} stands for the observed speed obtained from the HFI technique.

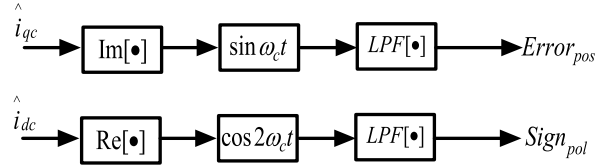


FIGURE 2. Heterodyning process to extract angle and polarity.

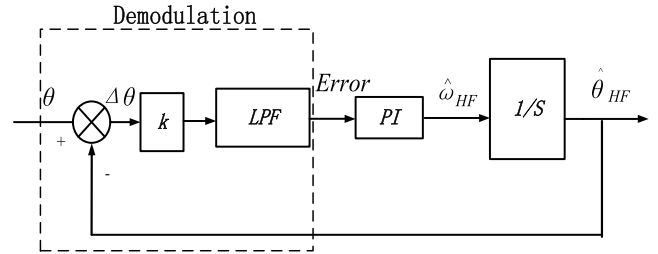


FIGURE 3. Tracking loop used for the rotor position estimation.

B. BEMF BASED STATE OBSERVER IN HIGH-SPEED REGION

The BEMF in the estimated rotor frame is

$$\begin{cases} \hat{e}_d = \omega_r \psi_m \sin \tilde{\theta}_r \\ \hat{e}_q = \omega_r \psi_m \cos \tilde{\theta}_r \end{cases} \quad (8)$$

where $\tilde{\theta}_r = \theta_r - \hat{\theta}_r$.

The estimated BEMF along the d-axis has the same form as the position error term of HFI scheme. So e_d could be used as the input of a PLL-based tracking controller to drive the estimated angle to the true value. When angle error $\tilde{\theta}_r = \theta_r - \hat{\theta}_r$ is very small, assuming the rotor speed and position remain constant during one control cycle, we can formulate the system state variables as:

$$\begin{cases} \dot{x} = Ax + Bu \\ y = Cx \end{cases} \quad (9)$$

where

$$\begin{aligned} x &= [\hat{i}_{ds} \quad \hat{i}_{qs} \quad \hat{e}_d \quad \hat{e}_q]^T \quad u = [\hat{V}_{ds} \quad \hat{V}_{qs}]^T \\ y &= [\hat{i}_{ds} \quad \hat{i}_{qs}]^T \\ A &= \begin{bmatrix} -\frac{R_s}{L_d} & \hat{\omega}_r \frac{L_q}{L_d} & \frac{1}{L_d} & 0 \\ -\hat{\omega}_r \frac{L_d}{L_q} & -\frac{R_s}{L_q} & 0 & -\frac{1}{L_q} \\ 0 & 0 & 0 & 0 \\ 0 & 0 & 0 & 0 \end{bmatrix} \quad B = \begin{bmatrix} \frac{1}{L_d} & 0 \\ 0 & \frac{1}{L_q} \\ 0 & 0 \\ 0 & 0 \end{bmatrix} \\ C &= \begin{bmatrix} 1 & 0 & 0 & 0 \\ 0 & 1 & 0 & 0 \end{bmatrix} \end{aligned}$$

An asymptotic state observer is employed. The observer can be described as:

$$\dot{x}^r = Ax^r + Bu + L(y - Cx^r) \quad (10)$$

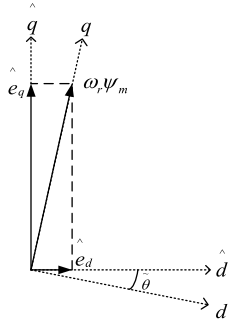


FIGURE 4. Actual vs observed back EMF in the sensorless control.

where

$$L = \begin{bmatrix} -\frac{R_s}{L_d} + 2\zeta\omega_0 & \frac{L_d}{L_q}\hat{\omega}_r \\ -\frac{L_q}{L_d}\hat{\omega}_r & -\frac{R_s}{L_q} + 2\zeta\omega_0 \\ L_d\omega_0^2 & 0 \\ 0 & -L_q\omega_0^2 \end{bmatrix}$$

ω_0 is the bandwidth of the observer, ζ is the damping coefficient. With a designed gain matrix L , the observer generates the observed vector x^T , containing the estimated BEMF, as shown in Fig. 5.

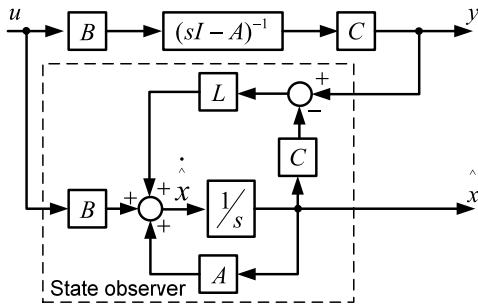


FIGURE 5. State observer to estimate back EMF.

C. HYBRID OBSERVER IN TRANSITION REGION

To realize the full-speed-range sensorless control, HFI and BEMF are combined by using a hybrid observer. The error information obtained from HFI scheme and BEMF based method has the identical form: $error = K \sin \hat{\theta}_r$. These two error signals could be used for the PLL-based tracking controller with the necessary normalization. A new error signal which combined these two together is defined by (9). $f_{tr}(\hat{\omega}_r)$ is a transition function that determines which error signal should be relied on, as shown in Fig. 6.

$$error = f_{tr}(\hat{\omega}_r) \frac{err_{pos}}{2K_{LS}} + [1 - f_{tr}(\hat{\omega}_r)] \frac{e_d}{K_{HS}} \quad (11)$$

where $K_{LS} = \frac{V_2}{4\omega_c} (\frac{L_q - L_d}{L_d L_q})$, $K_{HS} = \omega_r \psi_m$.

The block diagram of hybrid observer is shown in Fig. 7. A PLL-based tracking controller is used. Since this paper is

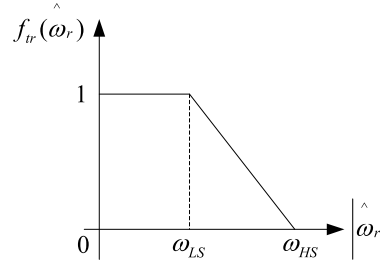


FIGURE 6. Transition function.

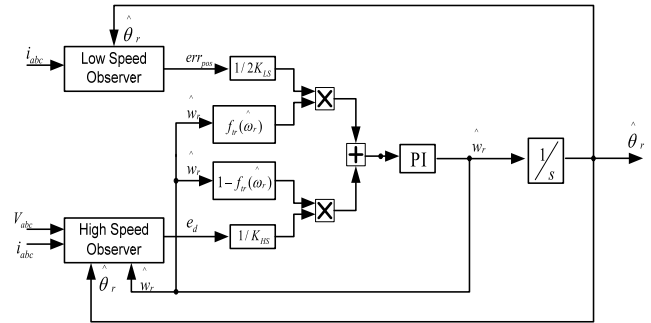


FIGURE 7. Hybrid observer block diagram.

focused on the HFI method, we will not detail the BEMF and the hybrid observer.

D. THE SELECTION OF THE INJECTION FREQUENCY

Due to the limitation of conventional micro-controllers and power devices, the switching frequency of the motor drive system is only 5-10 kHz, which explains why majority of injection frequency falls into the range of 500~1000 Hz. The room between the switching frequency and injection frequency is limited, which restrains the design of the filter. Our study will apply a simple first-order LPF design. Here ω_{cut} is the cut-off frequency.

$$\begin{cases} |H(j\omega)| = \frac{1}{\sqrt{1 + (\frac{\omega}{\omega_{cut}})^2}} \\ \angle H(j\omega) = -\tan^{-1}(\frac{\omega}{\omega_{cut}}) \end{cases} \quad (12)$$

If ω_{cut} is close to the injection frequency, the position signal will be distorted in terms of the phase and amplitude, which jeopardizes the precision of estimation. If ω_{cut} is near the switching frequency, where the harmonics are severe, it also worsens the estimated position. Therefore, it is preferred to leave enough gap between the motor fundamental frequency, injected frequency and the switching frequency.

Note both the fundamental waveform (voltage and current) and the injected harmonics will be modulated by the PWM strategy, e.g., comparing the reference with carrier triangles and generating the switch duty cycle. Therefore both the fundamental and the injected signal carry harmonics. When the motor is running at high speed with relatively low-frequency injected signal, as shown in Fig. 8 where the

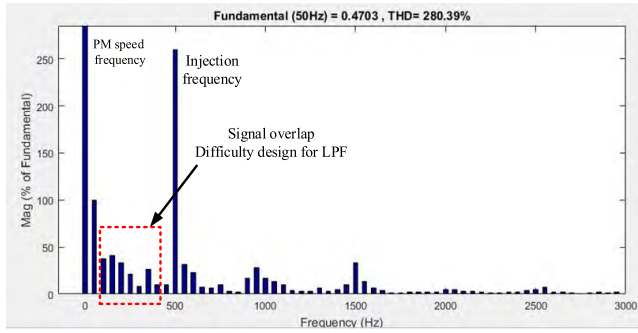


FIGURE 8. The motor current spectrum at 500Hz injection frequency.

injection frequency is 500Hz, potentially some of the low-order current harmonics will be overlapped with the injected-frequency fundamental component. Even an excellent filter cannot 100% separate all these signals. When the speed of motor goes up, such overlap becomes worse.

In Fig. 9 where the injection frequency is 2 kHz, the overlap between injection frequency and fundamental frequency is little, which results in the fidelity of position information even for the higher speed. Of course this requires a higher switching frequency. To set the injection frequency of 2 kHz, 10 kHz switching frequency is not enough anymore. SiC devices will be the candidate for > 10 kHz switching in high-power applications.

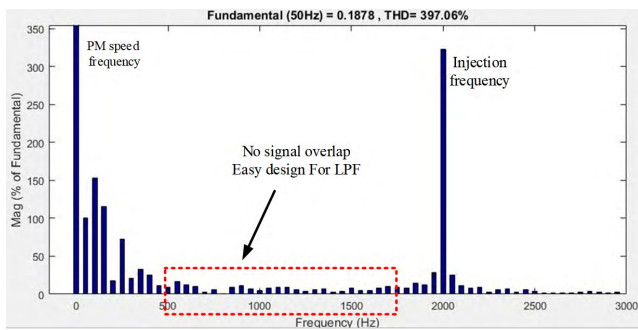


FIGURE 9. The motor current spectrum at 2 kHz injection frequency.

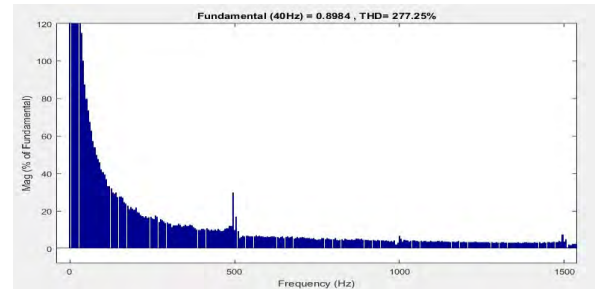
While conventional analysis regards the BEMF of the motor as the pure sinusoidal waveform, the motor has slotting effect, resulting in uneven magnetic conductance. The interaction between magnet motive force and non-uniform magnetic conductance induces the slotting harmonic EMF. When the motor rotates, the average magnetic conductance is periodic pulsation with the time of going through a tooth pitch, yielding the magnetic guiding wave as

$$\lambda(\theta, t) = (A_0 + \sum A_i \cos(i \frac{Z}{p} \omega_f t)) + \sum A_j \cos(j \frac{Z}{p} \theta) \quad (13)$$

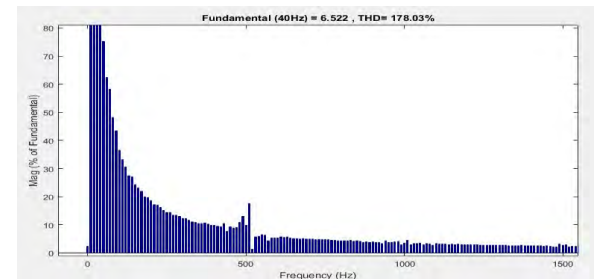
where Z is the number of stator slots, p is the pole pair of the motor, $A_0 + \sum A_i \cos(iZ/p\omega_f t)$ is the average magnetic conductance, A_j is the amplitude of subharmonic magnetic

conductance, θ is position angle and ω_f is the fundamental angular velocity.

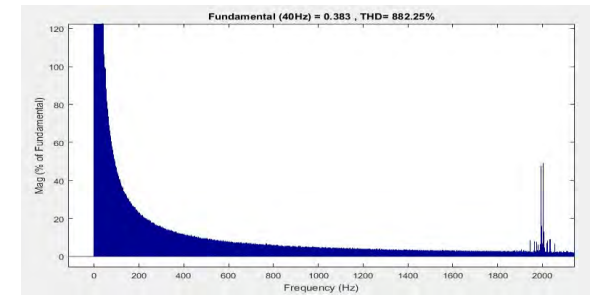
It can be seen from (13) that slotting harmonics can rapidly reach the HFI frequency with the increase of speed, which seriously confuses the extraction of the injected signal. Detailed simulation is carried out in Fig. 10.



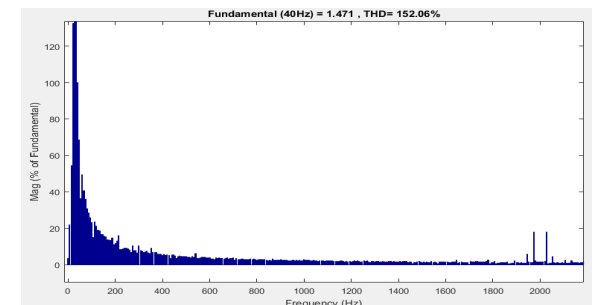
(a)



(b)



(c)



(d)

FIGURE 10. Relation between the effective injection signals with different motor speed at the same injected amplitude in three phase current. (a) 20 rpm & 500 Hz HFI. (b) 400 rpm & 500 Hz HFI. (c) 150 rpm & 2 kHz HFI. (d) 800 rpm & 2 kHz HFI.

From the simulation in Fig. 10, it can be seen that for the same signal injection amplitude, when the motor speed is low, even the low frequency signal injection still has a good signal-to-noise ratio. When the motor speed is increased,

the harmonics of back EMF greatly reduces the signal-to-noise ratio of the effective signal, resulting in HFI failure. When the injected signal is at higher frequency, the back EMF harmonics will not affect the signal-to-noise ratio of the injected signal. This is in aligned with the previous theoretical analysis.

The challenge then becomes the selection of the injection frequency. When the injection frequency increases, the inductive impedance of the three-phase motor will increase accordingly ($X_L = \omega L_m$). To keep the same-amplitude injected current, we need increase the amplitude of the injected voltage, which may cause modulation index > 1, i.e., over modulation. Since the injection frequency is much higher than the fundamental frequency, it is assumed that the fundamental frequency and BEMF are almost constant regardless of the injection signal. In addition, for simplicity of the analysis, the injection signal is replaced with the representative sinusoidal voltage ($A \cdot \sin \omega_c t$). Therefore in the steady state the injected HF current is:

$$i_c = \frac{A}{\sqrt{R_a^2 + (\omega_c L_m)^2}} \sin(\omega_c t - a \tan \frac{\omega_c L_m}{R_a}) \quad (14)$$

where R_a is phase internal resistance of PMSM, L_m is the motor leakage inductance, i_c is the injected current, A is the amplitude of the injected voltage, and ω_c is injection frequency. Assume the maximum modulation index is 1, the fundamental angular velocity is ω_0 and k is the phase electromotive coefficient ($V_{rms}/rad/s$). The amplitude of injected and fundamental voltage should not go beyond the DC-bus limit, i.e.,

$$A + \sqrt{2}k\omega_0 \leq \frac{V_{DC}}{\sqrt{3}} \quad (15)$$

Combining (14) and (15) yields (16), setting the limit between the fundamental and the injected frequency.

$$\sqrt{R_a^2 + (\omega_c L_m)^2} i_c + \sqrt{2}k\omega_0 \leq \frac{V_{DC}}{\sqrt{3}} \quad (16)$$

Following figures show simulation results of the estimation error under 2 kHz and 10 kHz injection frequency scenarios. The switching frequency is 100 kHz and the motor speed is 300 rpm. It can be seen that higher injection frequency can avoid signal noise caused by high speed and reduce the estimation error effectively. When the injection frequency is 2 kHz, the error is obviously greater than that of injection frequency 10 kHz, though such error might be acceptable in the applications.

E. IMPACT OF THE CONTROL BANDWIDTH

While it has been widely accepted that the higher the switching frequency the better the modulation performance, which can be simply realized by SiC devices over conventional Si devices, in this section we will focus on the control bandwidth, i.e., the updating speed of the algorithm. This has not been fully covered in previous literatures yet.

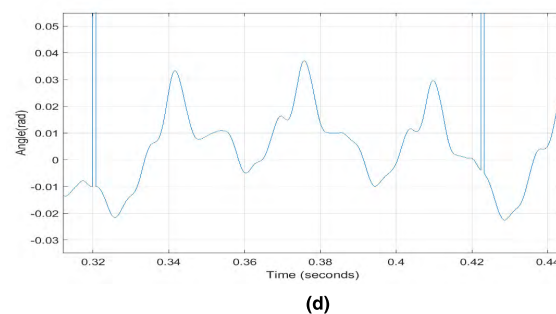
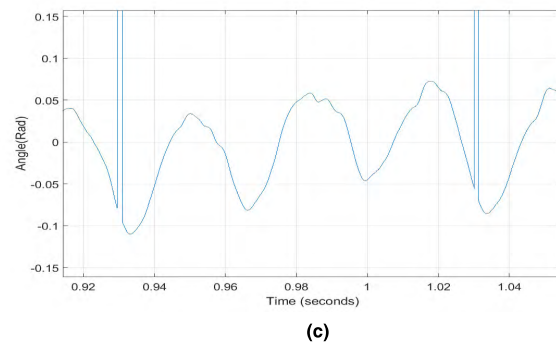
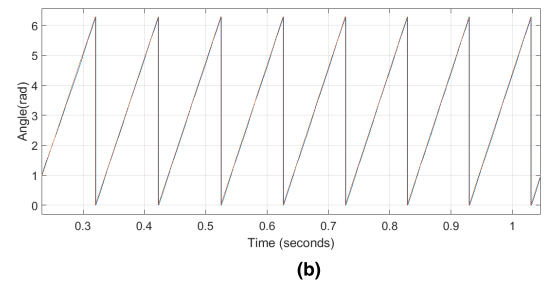
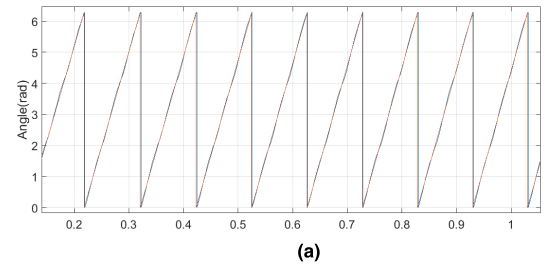


FIGURE 11. Estimation and errors with different injection frequency under the switching frequency 100 kHz and the speed 300rpm. (a) Estimation with 2 kHz injection frequency (yellow curve: estimation angle). (b) Estimation with 10 kHz injection frequency (yellow curve: estimation angle). (c) Angle error with 2 kHz injection frequency. (d) Angle error with 10 kHz injection frequency.

As shown in Fig. 12, a schematic diagram of different trigonometric waves (determining switching frequency) generated by the up/down counter and different control bandwidth generation of SVPWM, the faster the updating rate (green signal) the finer the tuned signal, yielding smaller harmonics. Sometimes the switching frequency can be high, however, the control performance is still not satisfactory if the updating rate (control bandwidth) is low.

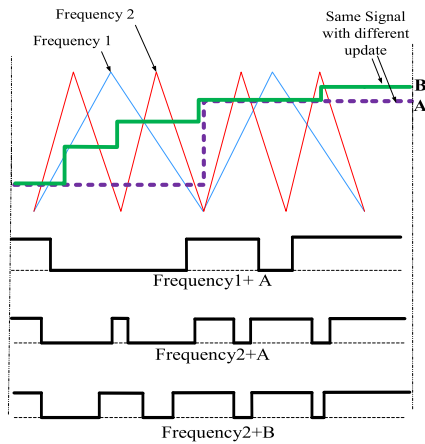


FIGURE 12. Impact of the control bandwidth.

Fig. 13 is the spectrum contrasts of the motor phase current. Both have 100 kHz switching frequency and 2 kHz injected signals. Their control bandwidth is different, i.e., 10 kHz and 100 kHz, respectively. Obviously, the higher the control bandwidth, the cleaner the signal thereby the easier to extract the useful signal.

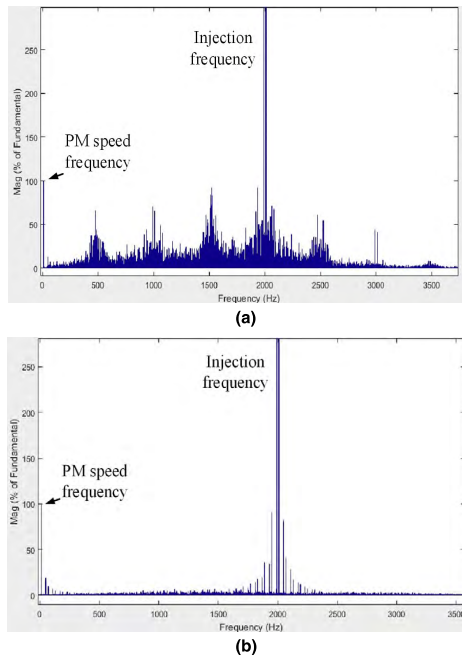


FIGURE 13. Impact of the different control bandwidth. (a) With the control bandwidth of 10 kHz. (b) With the control bandwidth of 100 kHz.

Assume the current of the q-axis after the high frequency injection contains following components:

$$\begin{cases} i_f^q = \frac{V_f^q}{Z_q} \sin(\omega_f t) \\ i_c^q = \frac{V_c^q}{Z_q} \sin(\omega_c t) \\ i_{PWM}^q = \frac{V_{PWM}^q}{Z_q} \sin(\omega_{PWM} t) \end{cases} \quad (17)$$

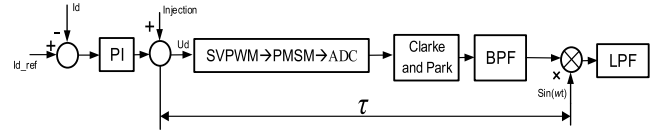


FIGURE 14. Delay caused by control bandwidth.

Here Z_q is the three-phase equivalent impedance in the d-q system. V_f^q, V_c^q, V_{PWM}^q are effective voltage after the modulation in d-q system. $\omega_f, \omega_c, \omega_{PWM}$ are the fundamental frequency, the injection frequency and the switching frequency of the inverter, respectively. i_f^q is the fundamental current of q-axis, i_c^q is the current component of the injection signal in the q-axis, i_{PWM}^q is the high frequency harmonic component introduced by the switching frequency. (13) multiplied by $\sin(\omega_c t)$ yields:

$$\begin{aligned} i_f^q \sin(\omega_c t) &= \frac{V_f^q}{Z_q} \sin(\omega_f t) \sin(\omega_c t) \\ &= \frac{V_f^q}{Z_q} (\cos(\omega_c - \omega_f)t - \cos(\omega_c + \omega_f)t) \end{aligned} \quad (18)$$

$$i_c^q \sin(\omega_c t) = \frac{V_c^q}{2Z_q} (\cos(2\omega_c t) - 1) \quad (19)$$

$$\begin{aligned} i_{PWM}^q \sin(\omega_c t) &= \frac{V_{PWM}^q}{Z_q} \sin(\omega_{PWM} t) \sin(\omega_c t) \\ &= \frac{V_{PWM}^q}{Z_q} (\cos(\omega_{PWM} - \omega_c)t \\ &\quad - \cos(\omega_{PWM} + \omega_c)t) \end{aligned} \quad (20)$$

With the influence of the control bandwidth, $\sin\omega_c t$ is delayed at least for τ . Here τ is the updating period, the inverse of the updating frequency. This applies to the injected signal, PWM and Analog-to-Digital Converter (ADC). The lower the control bandwidth, the bigger value of τ .

$$\begin{aligned} \frac{V_c^q}{Z_q} \sin(\omega_c t) \sin(\omega_c t - \tau) \\ = \frac{V_c^q \cos \tau}{2Z_q} (\cos 2\omega_c t - 1) - \frac{V_c^q \sin \tau}{2Z_q} \sin 2\omega_c t \end{aligned} \quad (21)$$

(21) shows in the non-ideal case, the delay τ not only reduces the effective signal intensity $-V_c^q \cos \tau / 2Z_q$, but also creates more harmonic components. This is consistent with the simulation results in Fig. 13.

As a summary, the ideal setting of related frequency is shown in Fig. 15, which describes the frequency relation of the fundamental wave, the LPF, the injection signal, the inverter switch and the control logic. It indicates:

1) A high control bandwidth reduces the distortion of the fundamental and injection signals, which in return reduces the effort of the filter design. Because FPGA is good at parallel processing, it greatly shortens the operation time of the FOC algorithm thereby allowing the switch duty cycle to be updated every switching period. This has been simulated in Fig.13 able to improve the signal to noise ratio

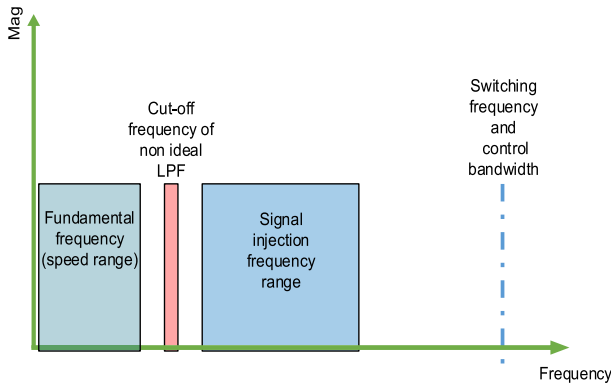


FIGURE 15. The relationship among fundamental frequency, cut-off frequency of LPF, switching frequency and control bandwidth.

of the injected signal, thereby ease of the position signal extraction.

2) A high switching frequency allows the wide range of the injection frequency and motor fundamental frequency. By using SiC devices, the inverter can endure high switching frequency. Not only the weight and volume of passive components but also the motor size can be greatly shrunk [37]. In addition to allowing higher injection frequency and widening the control bandwidth, SiC devices also adopts smaller dead band, which reduces the phase-current distortion. During the dead band, the top and bottom semiconductor devices are both off, with the current commutating through the body diode. The voltage error caused by dead band in each PWM cycle is

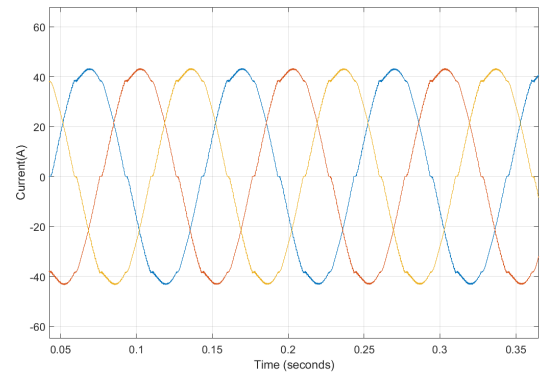
$$\Delta V_p = \frac{T_d + T_{on} - T_{off}}{T} V_d \quad (22)$$

Here T_d is dead band, T_{on} is turn-on interval for devices, T_{off} is turn-off interval for devices, T is the switching period, V_d is DC bus voltage. Since SiC devices have much shorter turn-on and turn-off delays, the dead band can be set as ~ 200 ns or even shorter, in contrast to $> 1\mu s$ in Si inverters. The following simulation results (Fig. 16) show that a short dead band reduces the distortion of the phase current.

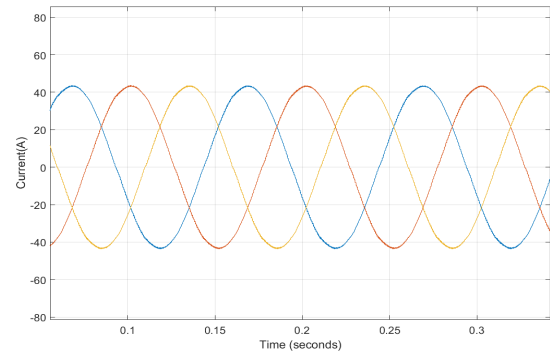
III. SYSTEM MODELING BASED ON XSG TOOLBOX

In this paper, the model-based design (MBD) method is utilized for the FOC algorithm, as shown in Fig. 17.

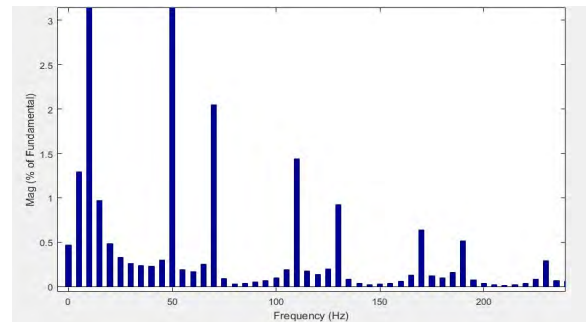
Since the FPGA supports a modular design, we divided the FOC algorithm into four modules (stages), with each module being built in the Simulink using XSG toolbox. Then the VHDL code for the FPGA can be automatically generated. The model is built from the Xilinx conventional module embedded in Matlab, aiming at the ease maintenance and fast development. Vivado will then burn functions into the FPGA and form a logical hardware array. At the same time, we can also see FPGA resources consumed by the entire algorithm, as shown in Fig. 18. The HFI sensorless control only occupies small portion of the FPGA.



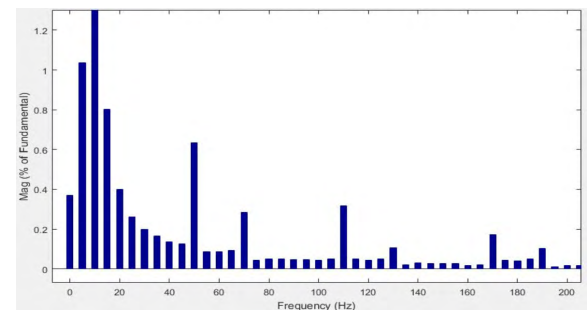
(a)



(b)



(c)



(d)

FIGURE 16. Phase current Impact from the dead band. (a) Three phase current with the dead band of $2\mu s$. (b) Three phase current with the dead band of 250 ns. (c) Three phase current harmonics with the dead band of $2\mu s$. (d) Three phase current harmonics with the dead band of 250 ns.

IV. HARDWARE EXPERIMENTAL RESULTS

In order to verify the effectiveness of the proposed design, the hardware setup is shown in Fig. 19, which contains a

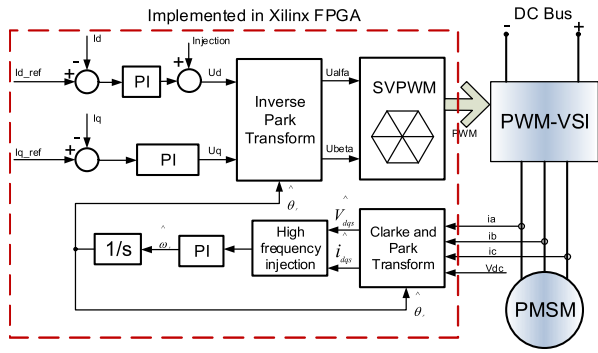


FIGURE 17. Control diagram of whole system.

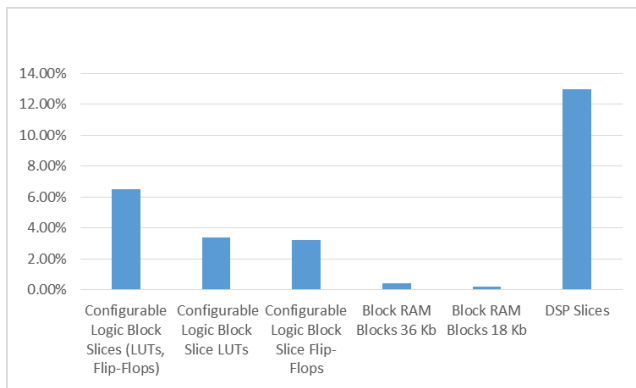


FIGURE 18. The occupancy and FPGA utilization.

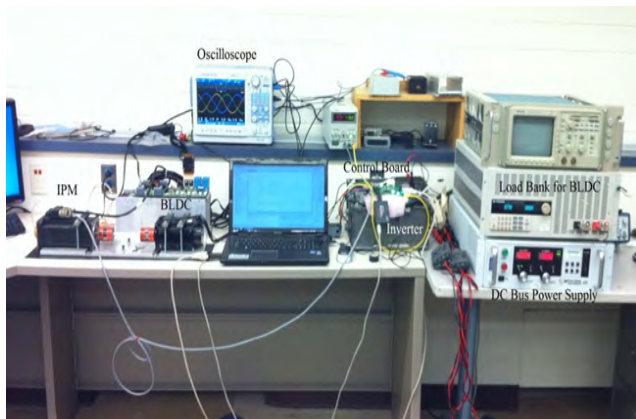
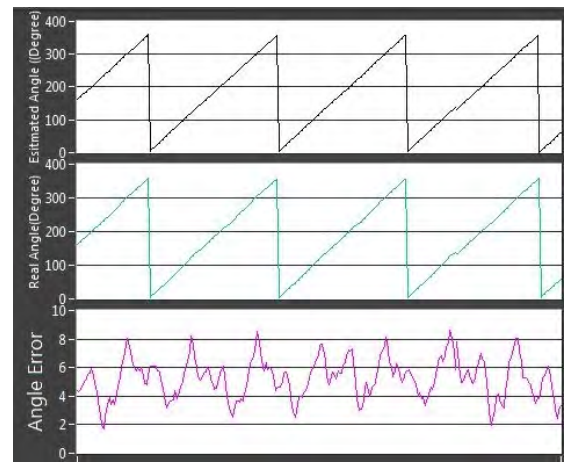


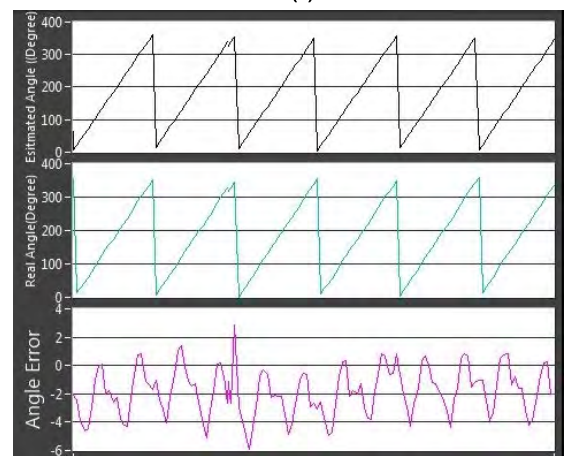
FIGURE 19. Experimental platform.

SiC-based three-phased inverter, one IPMSM and one MicroAutoBox with Xilinx XC7K325 FPGA chip embedded. Parameters of the tested IPMSM are presented in Table I. Test results, primarily the actual and estimated angle, can be obtained from the control desk provided by dSPACE. In the experiment, we set the control bandwidth equal to the switching frequency.

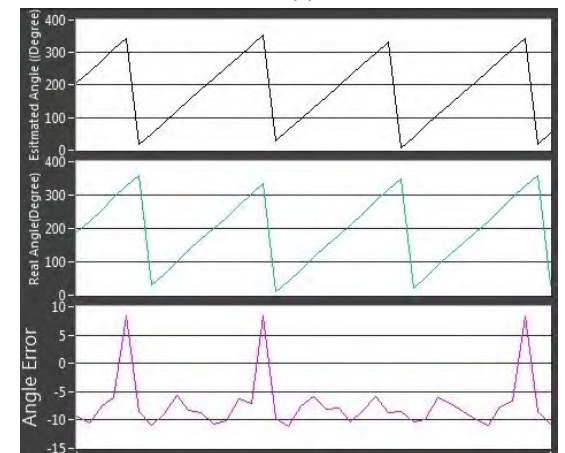
In Fig. 20, when the injection frequency is 500 Hz and motor speed is 32.5 rpm, we can use HFI to estimate the angle as shown in (a), indicating the angle error of 8°. When the speed increases to 139 rpm, the angle error becomes



(a)



(b)



(c)

FIGURE 20. Using hybrid controller for angle estimation. (a) Estimated at 32.5 RPM, using HFI method. (b) Estimated at 139 RPM, using HFI + Back EMF. (c) Estimated at 295 RPM, using pure back EMF.

larger and the control needs transition from HFI to BEMF, using the hybrid observer. When the speed goes to 295 rpm, the angle is solely estimated by the BEMF observer with the HFI disabled.

With experiments carried out under 2 kHz injection frequency and 100 kHz switching frequency, Fig. 21 shows

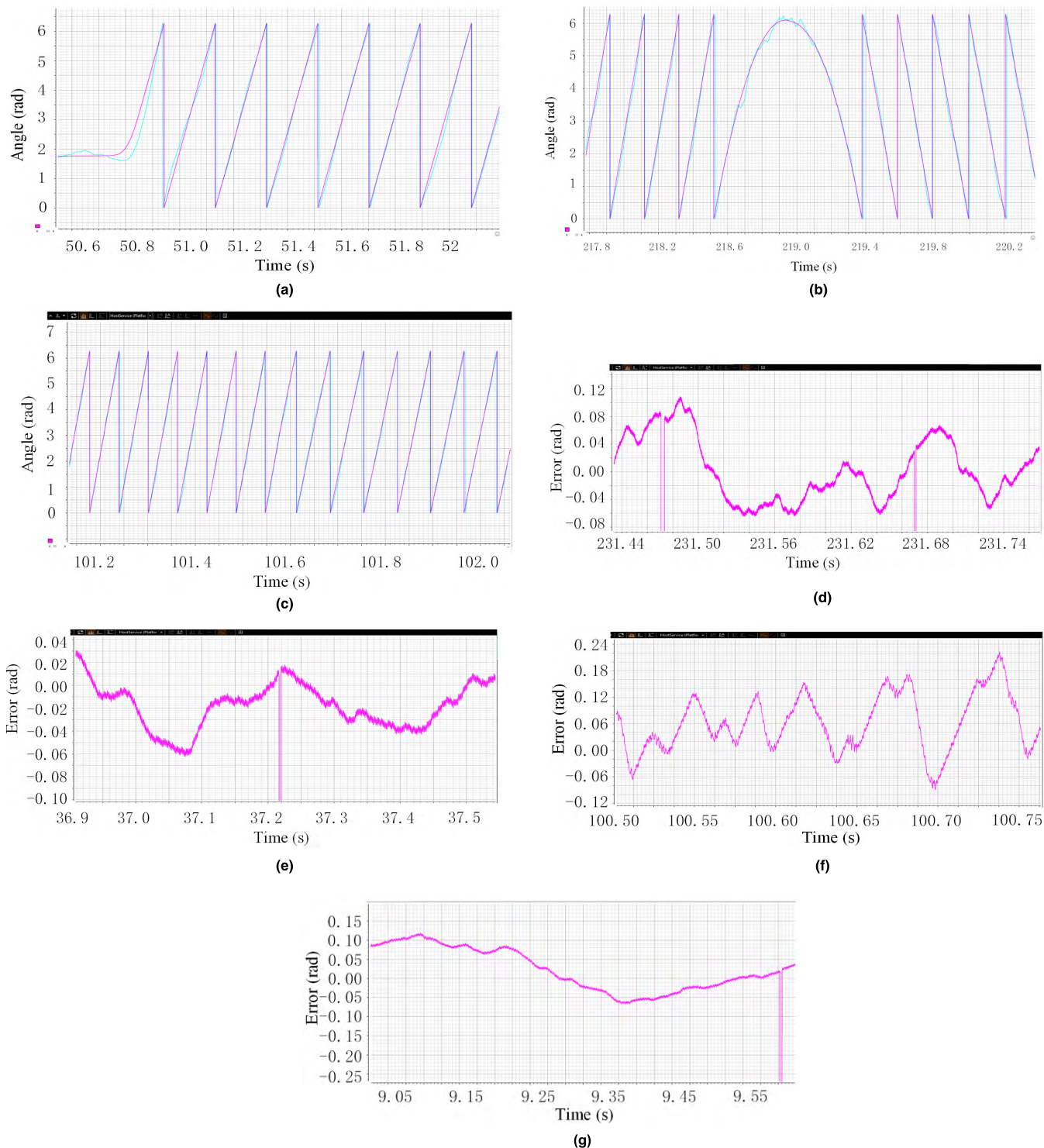


FIGURE 21. Position estimation and estimation error. (a) The position estimation under 300 rpm. (b) The position estimation when reversing the direction. (c) The position estimation under 1200 rpm. (d) Estimation error with 500 Hz injection at 300 rpm electrical angle. (e) Estimation error with 2000 Hz injection at 600 rpm electrical angle. (f) Estimation error with 500 Hz injection at 1200 rpm electrical angle. (g) Estimation error with 2000 Hz injection at 1200 rpm electrical angle.

the comparison between actual and estimated position under speed of 300 rpm, forward and reverse rotation and 1200 rpm, respectively. The purple signal is the real position

whereas the blue signal is the estimated position. The error between the real and estimated position when motor speed is 1200 rpm is <math><2.3\%</math>. No hybrid or BEMF observer is needed.

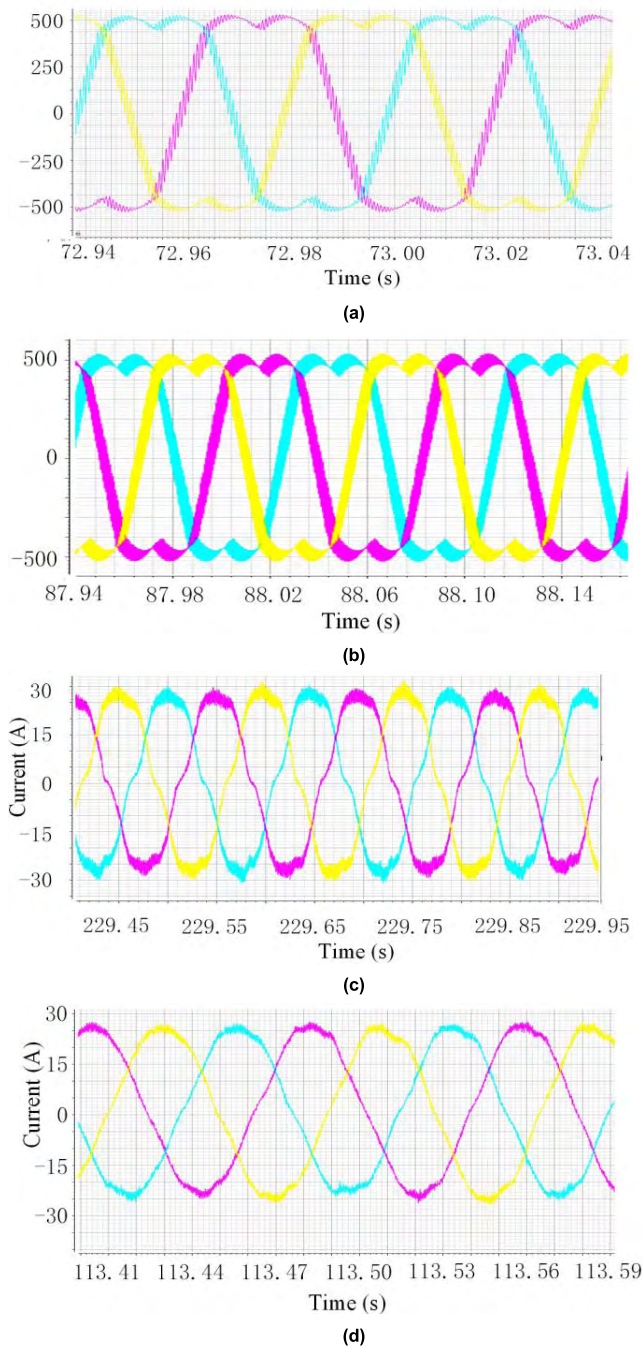


FIGURE 22. Three-phase duty cycle signals and current. (a) Three-phase duty cycle signals with 500 Hz injection. (b) Three-phase duty cycle signals with 2000 Hz injection. (c) Three-phase current ripple under 500 Hz injection frequency. (d) Three-phase current under 2 kHz injection frequency.

Experimental results verified that the estimated angle is well aligned with the experimental data.

Fig. 22 shows reference waveforms under the HFI method. They are compared with the triangle wave to produce the PWM, which is used to control three phase inverters. Due to the injection of high frequency signals, the reference waveform is superimposed with the injection signal. The signal

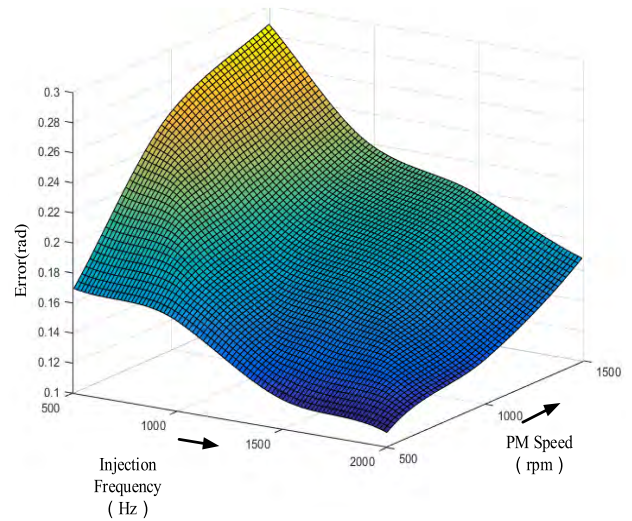


FIGURE 23. The relationship among error, injection frequency and PMSM speed.

TABLE 1. Parameters of tested PMSM.

Item	Value	Unit
Rated Voltage	230	V
Current Continuous	3.0	A
Current Peak	9.6	A
Rated Power	6.9	kW
Max Speed	3800	rpm
Rated Torque	2.44	Nm
Peak Torque	7.38	Nm
d-axis inductance	12	mH
q-axis inductance	34	mH
Stator Resistance	6.98	Ω

component will also be involved in the modulation. The yellow, blue and purple lines are reference waveforms of three phases. Furthermore, the injected voltage harmonics is imposed to the fundamental, yielding the fuzzy three-phase duty cycle signals.

Experimental results were summarized as Fig. 23.

It shows the relationship among error of the angle estimation, injection frequency and speed. It can be concluded that with the increasing of the injection frequency, the precision of the position estimation increases too. In addition, within the tolerable angle estimation error, the higher the injection frequency the wider the applicable range of speed using the HFI sensorless control. Furthermore, Fig. 24 is the curved surface based on the experimental data, showing the relationship among error of angle estimation, switching frequency, control bandwidth and injection frequency. Increasing either the switching frequency (control bandwidth) or injection frequency will improve the precision of estimation. Note the experiment sets the switching frequency equal to the control bandwidth.

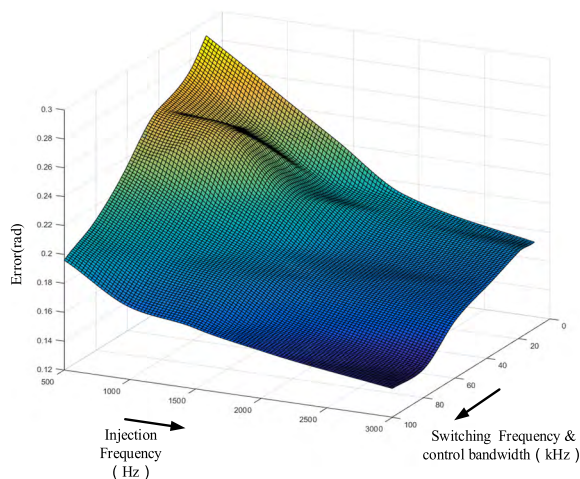


FIGURE 24. Angle error, switching frequency (control bandwidth) and injection frequency.

V. CONCLUSIONS

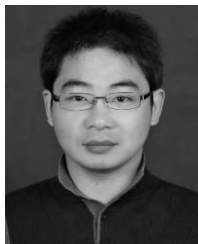
This paper presented a high-frequency injection sensorless position estimation by using FPGA and SiC inverter. Due to the fastness and high compactness of FPGA, the control bandwidth can be much higher than most of conventional microcontroller. The high switching frequency and control bandwidth together make the high injection frequency (~ 2 kHz) possible and in result secure both the high precision of position estimation and the wide applicable range of the motor speed. Experimental results validated the effectiveness of proposed sensorless position estimation in FPGA. The resources occupied inside the FPGA was calculated as well.

Given the advantage of SiC devices is well known in power electronics domain, we skipped the discussion of the SiC inverter and only focused on the wide control bandwidth of FPGAs. From this aspect, this paper proves that the high control bandwidth of FPGAs effectively maximizes the high-switching-frequency capability of wide-bandgap semiconductors. Though this paper has lifted the injection frequency to 2 kHz, the future work is to seek the optimal injection frequency of the sensorless control.

REFERENCES

- [1] C. R. Harahap, R. Saito, H. Yamada, and T. Hanamoto, "Speed control of permanent magnet synchronous motor using FPGA for high frequency SiC MOSFET inverter," *J. Eng. Sci. Technol.*, pp. 11–20, Oct. 2014.
- [2] P. K. Sharma and A. S. Sindekar, "Performance analysis and comparison of BLDC motor drive using PI and FOC," in *Proc. Int. Conf. Global Trends Signal Process., Inf. Comput. Commun. (ICGTSP/ICC)*, Jalgaon, India, Dec. 2016, pp. 485–492.
- [3] F. Genduso, R. Miceli, C. Rando, and G. R. Galluzzo, "Back EMF sensorless-control algorithm for high-dynamic performance PMSM," *IEEE Trans. Ind. Electron.*, vol. 57, no. 6, pp. 2092–2100, Jun. 2010.
- [4] X. Song, B. Han, S. Zheng, and J. Fang, "High-precision sensorless drive for high-speed BLDC motors based on the virtual third harmonic back-EMF," *IEEE Trans. Power Electron.*, vol. 33, no. 2, pp. 1528–1540, Feb. 2018.
- [5] R. G. Krishnan, T. B. Isha, and P. Balakrishnan, "A back-EMF based sensorless speed control of permanent magnet synchronous machine," in *Proc. Int. Conf. Circuit, Power Comput. Technol. (ICCPCT)*, Kollam, India, Apr. 2017, pp. 1–5.
- [6] S. Halder, P. Agarwal, and S. P. Srivastava, "MTPA based sensorless control of PMSM using position and speed estimation by back-EMF method," in *Proc. Int. Conf. Power Syst. (ICPS)*, New Delhi, India, Mar. 2016, pp. 1–4.
- [7] G. Liu, C. Cui, K. Wang, B. Han, and S. Zheng, "Sensorless control for high-speed brushless DC motor based on the line-to-line back EMF," *IEEE Trans. Power Electron.*, vol. 31, no. 7, pp. 4669–4683, Jul. 2016.
- [8] C. Zhou, C. Xie, and M. Zhang, "Speed-sensorless control for induction motor based on back-EMF integration," in *Proc. Conf. Ind. Electron. Appl. (ICIEA)*, Auckland, New Zealand, Jun. 2015, pp. 1376–1379.
- [9] J.-W. Lee, "Adaptive sensorless control of high speed PMSM with back EMF constant variation," in *Proc. Int. Conf. Power Electron. ECCE Asia (ICPE-ECCE Asia)*, Seoul, South Korea, Jun. 2015, pp. 1400–1404.
- [10] Y. Li, M. Yang, J. Long, Z. Liu, and D. Xu, "Current sensorless predictive control based on extended Kalman filter for PMSM drives," in *Proc. IEEE Transp. Electrific. Conf. Expo, Asia-Pacific (ITEC Asia-Pacific)*, Harbin, China, Aug. 2017, pp. 1–6.
- [11] D. Raca, M. C. Harke, and R. D. Lorenz, "Robust magnet polarity estimation for initialization of PM synchronous machines with near-zero saliency," *IEEE Trans. Ind. Appl.*, vol. 44, no. 4, pp. 1199–1209, Jul./Aug. 2008.
- [12] H. Kim, K.-K. Huh, R. D. Lorenz, and T. M. Jahns, "A novel method for initial rotor position estimation for IPM synchronous machine drives," in *Proc. Conf. Rec. IEEE IAS Annu. Meeting*, vol. 2, Oct. 2003, pp. 1173–1180.
- [13] M. Corley and R. D. Lorenz, "Rotor position and velocity estimation for a permanent magnet synchronous machine at standstill and high speeds," in *Proc. Conf. Rec. IEEE IAS Annu. Meeting*, vol. 1, Oct. 1996, pp. 36–41.
- [14] Y. Jeong, R. D. Lorenz, T. M. Jahns, and S. Sul, "Initial rotor position estimation of an interior permanent magnet synchronous machine using carrier-frequency injection methods," in *Proc. IEEE IEMDC*, Madison, WI, USA, Jun. 2003, pp. 1218–1223.
- [15] H. Kim, M. C. Harke, and R. D. Lorenz, "Sensorless control of interior permanent magnet machine drives with zero-phase lag position estimation," in *Proc. IEEE Int. Electr. Mach. Drives Conf. (IEMDC)*, Pittsburgh, PA, USA, Jun. 2002, pp. 1661–1667.
- [16] D. Raca, P. Garcia, D. D. Reigosa, F. Briz, and R. D. Lorenz, "Carrier signal selection for sensorless control of PM synchronous machines at zero and very low speeds," in *Proc. IEEE Ind. Appl. Soc. Annu. Meeting*, Oct. 2008, pp. 1–8.
- [17] J. M. Liu and Z. Q. Zhu, "Sensorless control strategy by square-waveform high-frequency pulsating signal injection into stationary reference frame," *IEEE J. Emerg. Sel. Topics Power Electron.*, vol. 2, no. 2, pp. 171–180, Jun. 2014.
- [18] D. Kim, Y.-C. Kwon, S.-K. Sul, J.-H. Kim, and R.-S. Yu, "Suppression of injection voltage disturbance for high-frequency square-wave injection sensorless drive with regulation of induced high-frequency current ripple," *IEEE Trans. Ind. Appl.*, vol. 52, no. 1, pp. 302–312, Jan./Feb. 2016.
- [19] P. L. Xu and Z. Q. Zhu, "Novel square-wave signal injection method using zero-sequence voltage for sensorless control of PMSM drives," *IEEE Trans. Ind. Electron.*, vol. 63, no. 12, pp. 7444–7454, Dec. 2016.
- [20] R. Ni, D. Xu, F. Blaabjerg, K. Lu, G. Wang, and G. Zhang, "Square-wave voltage injection algorithm for PMSM position sensorless control with high robustness to voltage errors," *IEEE Trans. Power Electron.*, vol. 32, no. 7, pp. 5425–5437, Jul. 2017.
- [21] A. Alaei, D.-H. Lee, J.-W. Ahn, and S. M. S. Nejad, "Dynamic performance analysis of high frequency signal injection based sensorless methods for IPM synchronous motors," in *Proc. Annu. Power Electron., Drives Syst. Technol. Conf. (PEDSTC)*, Feb. 2018, pp. 151–156.
- [22] E. Trancho et al., "A novel PMSM hybrid sensorless control strategy for EV applications based on PLL and HFI," in *Proc. 42nd Annu. Conf. IEEE Ind. Electron. Soc. (IECON)*, Florence, Italy, Oct. 2016, pp. 6669–6674.
- [23] D. Hind et al., "A hybrid sensorless control solution for an automotive drive application," in *Proc. IEEE Int. Electr. Mach. Drives Conf. (IEMDC)*, Miami, FL, USA, May 2017, pp. 1–6.
- [24] Z. Chen, Z. Zhang, R. Kennel, and G. Luo, "Hybrid sensorless control for SPMSM With multiple saliencies," in *Proc. 41st Annu. Conf. IEEE Ind. Electron. Soc. (IECON)*, Yokohama, Japan, Nov. 2015, pp. 1188–1193.
- [25] H. M. D. W. Habbib and A. A. A. Al-Khazraji, "FPGA based vector control of PM motor using sliding mode observer," in *Proc. Mod. Electr. Power Syst. (MEPS)*, Wroclaw, Poland, Jul. 2015, pp. 1–5.

- [26] S. Medjmadj, D. Diallo, M. Mostefai, C. Delpha, and A. Arias, "PMSM drive position estimation: Contribution to the high-frequency injection voltage selection issue," *IEEE Trans. Energy Convers.*, vol. 30, no. 1, pp. 349–358, Mar. 2015.
- [27] Y. Fan, R. Wang, and L. Zhang, "Sensorless control of five-phase IPM motor based on high-frequency sinusoidal voltage injection," in *Proc. Int. Conf. Elect. Mach. Syst. (ICEMS)*, Aug. 2017, pp. 1–5.
- [28] Z. Ma, J. Gao, and R. Kennel, "FPGA implementation of a hybrid sensorless control of SMPMSM in the whole speed range," *IEEE Trans. Ind. Informat.*, vol. 9, no. 3, pp. 1253–1261, Aug. 2013.
- [29] K. Shirabe et al., "Advantages of high frequency PWM in AC motor drive applications," in *Proc. IEEE Energy Convers. Congr. Expo.*, Raleigh, NC, USA, Sep. 2012, pp. 2977–2984.
- [30] Z. Zhou, T. Li, T. Takahashi, and E. Ho, "FPGA realization of a high-performance servo controller for PMSM," in *Proc. 19th Annu. IEEE Appl. Power Electron. Conf. Expo. (APEC)*, Feb. 2004, pp. 1604–1609.
- [31] Y. S. Kung and M. H. Tsai, "FPGA-based speed control IC for PMSM drive with adaptive fuzzy control," *IEEE Trans. Power Electron.*, vol. 22, no. 6, pp. 2476–2486, Nov. 2007.
- [32] T. Hanamoto, M. Deriha, H. Ikeda, and T. Tsuji, "Digital hardware circuit using FPGA for speed control system of permanent magnet synchronous motor," in *Proc. 18th Int. Conf. Elect. Mach. (ICEM)*, Sep. 2008, pp. 1–5.
- [33] R. Lai, L. Wang, J. Sabate, A. Elasser, and L. Stevanovic, "High-voltage high-frequency inverter using 3.3 kV SiC MOSFETs," in *Proc. 15th Int. Power Electron. Motion Control Conf. (EPE/PEMC)*, Novi Sad, Serbia, Sep. 2012, pp. DS2b.6-1–DS2b.6-5.
- [34] M. Shen, S. Krishnamurthy, and M. Mudholkar, "Design and performance of a high frequency silicon carbide inverter," in *Proc. IEEE Energy Convers. Congr. Expo. (ECCE)*, Phoenix, AZ, USA, Sep. 2011, pp. 2044–2049.
- [35] C. Lai, G. Feng, J. Tjong, and N. C. Kar, "Direct calculation of maximum-torque-per-ampere angle for interior PMSM control using measured speed harmonic," *IEEE Trans. Power Electron.*, to be published. [Online]. Available: <https://ieeexplore.ieee.org/document/8245818/>
- [36] J. Ma, J. Zhao, J. Sun, and C. Yan, "A novel PMSM speed control scheme based on sliding-mode and fuzzy disturbance observer," in *Proc. Annu. Conf. IEEE Ind. Electron. Soc. (IECON)*, Beijing, China, Nov. 2017, pp. 1704–1710.
- [37] Y. Li, D. Han, and B. Sarlioglu, "Design of high-speed machines using silicon-carbide based inverters," in *Proc. IEEE Energy Convers. Congr. Expo. (ECCE)*, Sep. 2015, pp. 3895–3900.



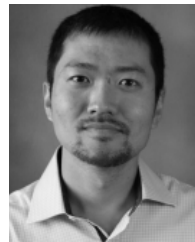
WEI QIAN received the B.S. degree in mechanical engineering and automation and the M.S. degree in aircraft design from the Nanjing University of Aeronautics and Astronautics, Nanjing, China, in 2005 and 2013, respectively. He is currently pursuing the Ph.D. degree with the School of Mechanical Engineering, Shanghai Jiao Tong University, Shanghai, China. His research interests include soft switching power converters, power electronics devices, and electric motor control systems.



XI ZHANG received the B.Sc. degree in applied mathematics, the B.E. degree in information and control engineering, and the M.E. and Ph.D. degrees in power electronics and electric power drive from Shanghai Jiao Tong University (SJTU), Shanghai, China, in 2002, 2004, and 2007, respectively. From 2007 to 2009, he held a post-doctoral position with the Department of Electrical and Computer Engineering, University of Michigan-Dearborn, Dearborn, MI, USA. He is currently an Associate Professor with the National Engineering Lab for Automotive Electronics and Control Technology, Institute of Automotive Engineering, SJTU. His research interests include power management strategies, power electronics devices, and electric motor control systems for alternative-fuel vehicles.



FANNING JIN (S'16) was born in China in 1992. He received the B.E. degree in automation from the Huazhong University of Science and Technology, Hubei, China, in 2015, and the M.S.E. degrees in electrical engineering from the University of Michigan-Dearborn, Dearborn, MI, USA, in 2017. His research interests include field-programmable gate array utilization in various control algorithm (e.g., motor control) and hybrid energy storage system for EV applications.



HUA BAI received the B.S. and Ph.D. degrees from the Department of Electrical Engineering, Tsinghua University, Beijing, China, in 2002 and 2007, respectively. He was a Post-Doctoral Fellow and also a Research Scientist with the University of Michigan-Dearborn, USA, in 2007 and 2009, respectively. He was an Assistant Professor with the Department of Electrical and Computer Engineering, Kettering University, Flint, MI, USA, from 2010 to 2016. From 2017 to 2018, he joined the University of Michigan-Dearborn as an Associate Professor. He is currently an Associate Professor with the EECS Department, The University of Tennessee at Knoxville. His research interests include power electronic modeling, control and integration including variable frequency motor drive system, high voltage and high power DC/DC converter, wide-bandgap devices, and hybrid electric vehicles.



DINGGUO LU (S'09–M'18) received the B.Eng. degree in mechanical engineering from Zhejiang University, Hangzhou, China, in 1997, the M.S. degree in mechanical engineering and the Ph.D. degree in electrical engineering from the University of Nebraska–Lincoln, Lincoln, NE, USA, in 2009 and 2018, respectively. He is currently an Engineer with the Mercedes-Benz Research and Development North America, Inc., Redford, MI, USA. His research interests include electric machines and drives, power electronics, renewable energy systems, and machine learning and its applications in hybrid-electric vehicles.



BING CHENG (S'90–M'97) received the B.S. and M.S. degrees from Northeastern University, Shenyang, China, in 1982 and 1984, respectively, and the Ph.D. degree from the University of Massachusetts at Amherst, in 1992, all in electrical engineering. From 1992 to 1994, he was with Cleveland Machine Controls, Inc., where he was responsible for the AC induction motor control development for industrial drives. In 1994, he joined Ford Motor Company—Ecostar Electric Drives, LLC, which was acquired by Ballard Power Systems, Siemens VDO, and Continental Corporation. As a Principal Engineer, he performed research and development work on motor control software development, power electronic, and system simulation for fuel-cell and hybrid vehicles. From 2010 to 2015, he was with Fiat Chrysler Automobiles as the E-Motor Controls and Integration Manager, where he was responsible for the motor control, motor calibration, and software development for all the battery/hybrid electric vehicles programs. In 2015, he joined Mercedes-Benz Research and Development North America as a motor control and calibration manager. He is currently responsible for the E-drive motor control research and software development for hybrid and electric vehicle applications. Since 2013, he has been an Adjunct Professor with the Electrical Engineering Department, McMaster University. His interests include control systems, electric machines, and power electronics in electric/hybrid vehicle applications.

...